J. Fluid Mech. (1976), *vol.* 77, *part* 4, *pp.* 709–735
Printed in Great Britain

On the spin-up and spin-down of a rotating fluid. Part 2. Measurements and stability

By PATRICK D. WEIDMAN
Department of Aerospace Engineering, University of Southern California, Los Angeles

(Received 27 March 1975 and in revised form 18 May 1976)

Measurements of the azimuthal velocity inside a cylinder which spins up or spins down at constant acceleration were obtained with a laser-Doppler velocimeter and compared with the theoretical results presented in part 1. Velocity profiles near the wave front in spin-up indicate that the velocity discontinuity given by the inviscid Wedemeyer model is smoothed out in a shear layer whose thickness varies with radius and time but scales with $hE_{\Omega}^{\frac{1}{4}}$. The spin-down profiles are always in excellent agreement with theory when the flow is stable. Visualization studies with aluminium tracers have made possible the determination of the stability boundary for Ekman spiral waves (principally type II waves) observed on the cylinder end walls during spin-up. For spin-down to rest the flow always experienced a centrifugal instability which ultimately disrupted the interior fluid motion.

1. Introduction

Perhaps the first comprehensive experimental study of spin-up is that of McLeod (1922). He made extensive velocity measurements of a fluid with a free surface in a cylindrical container which was both spun-up and spun-down impulsively and noted a departure from his purely diffusive theory which "increases with angular velocity and with the size of the cylinder, but which tends to vanish at very low speeds". Thus McLeod had already observed trends which are now known to scale with the Ekman number $E_{\Omega} = \nu/\Omega h^2$. Furthermore, he attributed the observed differences between theory and measurement to the "effect of the base". It took more than four decades before McLeod's astute observations were theoretically understood in the now classic paper of Greenspan & Howard (1963).

Recent measurements of spin-up in a cylinder at small Ekman numbers have been reported by Goller & Ranov (1968) for a fluid with a free surface and by Ingersoll & Venezian (1968) for a contained fluid. Both of these studies point out the usefulness of the Wedemeyer (1964) model for impulsive spin-up. The measurements of Watkins & Hussey (1976) for impulsive spin-up of a contained fluid are likewise in good agreement with velocity profiles computed from the full viscous Wedemeyer equation; in this experiment the Ekman numbers were in the range where the time scale changes smoothly from one of diffusion to one of convection.

The present investigation was initiated primarily to provide accurate experimental data to test the simplified solutions obtained from the extended Wedemeyer model in part 1. We consider only spin-up and spin-down at constant acceleration at Ekman numbers sufficiently small ($E_\Omega \sim 10^{-7}$) for the theory to be valid; moreover, the choice of acceleration rate is restricted so as to realize flows which are predominantly stable so that a fair comparison between theory and experiment can be made. The experimental apparatus is discussed in §2 and the velocity measurements are presented in §3.

Flow visualization carried out with aluminium-particle suspensions revealed that side-wall and end-wall instabilities could not always be avoided at the low Ekman numbers of interest. During spin-up one could clearly see spiral wave bands on the cylinder's end walls normally associated with instabilities in the Ekman boundary layer. Photographic records of these Ekman waves were obtained and the stability boundary, determined with the aid of the measured velocity profiles, is compared with observations available in the literature. To date, experimental investigations of type I waves (due to an inflexional instability) and type II waves (resulting from an interaction of shear and Coriolis forces) have been reported by Faller (1963), Faller & Kaylor (1965), Tatro & Mollo-Christensen (1967) and Caldwell & Van Atta (1970) for steady flows where the fluid rotates faster than the boundary. Smith (1947) and Gregory, Stuart & Walker (1955) have studied the instabilities which appear when a plate rotates beneath a stationary fluid, and at intermediate Rossby numbers only the single set of observations of Faller & Kaylor (1965) is known to the author. The present measurements help to fill in the gap at those intermediate Rossby numbers where the fluid rotates slower than the boundary. These data, as well as some observations of the spin-down centrifugal instability, are presented in §4. The results are discussed in §5 and concluding remarks are given in §6.

In the following presentation we shall use the same definitions as in part 1. We remind the reader that variables with an asterisk are dimensional and those without are non-dimensional. Also, equation numbers prefixed with I refer to the equations in part 1.

2. Experimental set-up

A schematic diagram of the experimental apparatus and data-acquisition equipment is presented in figure 1. The measurement system is broken down into the five components which are discussed briefly in the following subsections.

2.1. *Cylindrical container*

The cylindrical shell was turned from clear lucite stock to an inside diameter $2a = 15{\cdot}12$ cm and a height $h = 29{\cdot}18$ cm, thus giving an aspect ratio $A = h/a = 3{\cdot}86$. The inner and outer walls were machined parallel (to within $\pm\, 0{\cdot}003$ cm over the length) and then polished smooth. The cylinder ends were faced off flat and parallel (to within $\pm\, 0{\cdot}002$ cm over the diameter) to receive quality circular glass plates for flow visualization. The glass was sealed with rubber gaskets and held in place by plastic annular frames screwed into the ends

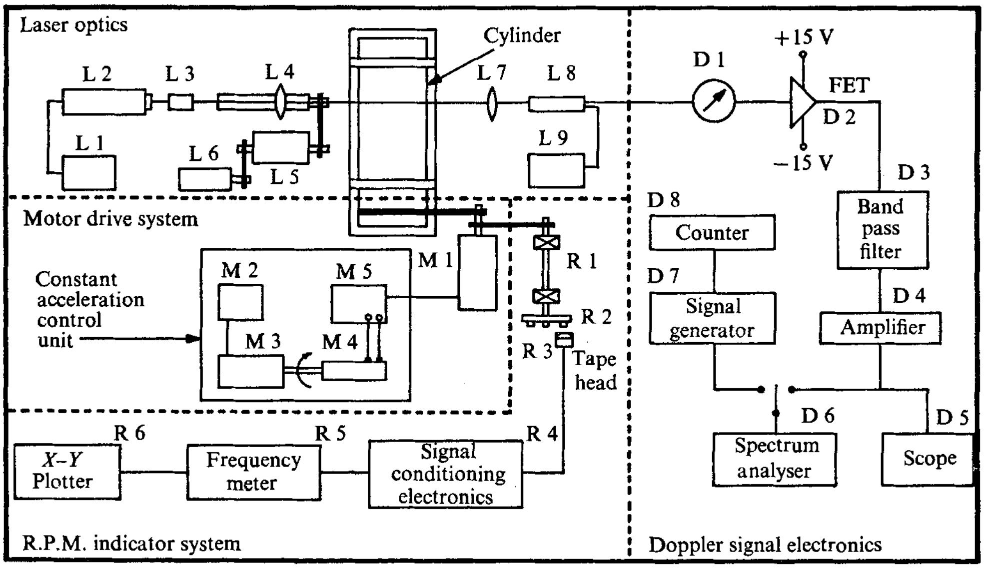

FIGURE 1. Diagram of experimental apparatus divided into four component systems: motor drive system, laser optics, Doppler signal electronics and r.p.m. indicator system.

of the cylinder. A shoulder approximately 5 cm in length was cut along each end of the cylinder to accept two thin-ring bearings pressed into place. A rigid aluminium frame supported the outer races of the bearings and final alignment, accomplished with the aid of shim stock, provided a smooth and freely turning cylinder. In operation, the cylinder was filled with distilled water and seeded with 0·5 μm polystyrene spheres to enhance radiation scattering for the laser-Doppler measurements.

Of primary importance in the experiment is the relative angle θ_w between the direction normal to the cylinder's end plates and the rotational axis. The theoretical treatment in part 1 presumes that there will be no stretching of the fluid vortex lines due to geometry. According to Pedlosky & Greenspan (1967), the end walls may be considered parallel as long as their slopes satisfy the relation

$$\theta_w \lesssim O(E_\Omega^{\frac{1}{2}}), \qquad (2.1)$$

where E_Ω is the Ekman number based on the maximum angular velocity. Careful measurements have shown that the average end-wall slopes could not have been greater than $\theta_w = 3{\cdot}2 \times 10^{-4}$ rad, and they were probably considerably less than this. The largest angular velocity encountered was 110 rad/s, which gives $E_\Omega^{\frac{1}{2}} = 2{\cdot}8 \times 10^{-4}$ for water at room temperature: thus the requirement (2.1) was adequately satisfied for all measurements reported here.

2.2. *Motor drive system*

The cylinder was belt driven by a reversible $\frac{1}{4}$ h.p. Bodine d.c. motor (denoted M 1 in figure 1), whose speed was monitored by a constant-acceleration control unit. This unit consisted of a variable speed control (M 2) regulating a $\frac{1}{70}$ h.p.

reversible motor (M 3) which in turn drove a 10-turn potentiometer (M 4) at a constant rate. The potentiometer regulated the current from the primary speed control (M 5) to the drive motor which then, theoretically, should accelerate the cylinder at a constant rate. The sign as well as the rate of acceleration could be set by the secondary speed control (M 2). Not shown in the diagram are the clutch and limit switches which helped to provide repeatable runs from one angular velocity to another.

In practice the cylinder speed curves always exhibited a small jump near zero velocity owing to the static friction of the system. Moreover, the acceleration rate for the drive motor under load varied significantly (deviations of 5–10 %) during a run. This problem was ameliorated by making one or two manual adjustments of the speed control (M 2) during the run; the linearity of the cylinder wall speed curve obtained in this manner had deviations of 1–3 % for spin-up and $\frac{1}{2}$–2 % for spin-down.

2.3. *R.p.m. indicator system*

The instantaneous speed of the cylinder was monitored electronically by the r.p.m. indicator system depicted in figure 1. Eight magnets were positioned at equal angles around the face of a plastic disk (R 2) mounted on a rotating shaft (R 1) which itself was geared to the drive motor. The irregular wave form picked up by the fixed magnetic tape head (R 3) was shaped into a rectangular pulse (R 4) and then fed into the frequency meter (R 5). A permanent velocity history of the cylinder wall was obtained by plotting the analog output voltage from the frequency meter against time on an X–Y pen recorder (R 6).

2.4. *Laser optics*

The laser-Doppler velocimeter was arranged in the self-focusing reference-beam mode originally used by Brayton (1969). In figure 1 we note the Optics Technology He–Ne CW laser (L 2) and its power supply (L 1), which together provided a coherent beam of 8 mW and ostensibly operated in a single axial TEM_{00} mode. A parallel-surface flat (L 3) split the incident radiation into two parallel beams which passed through a lens (L 4) to a common focal point inside the cylinder. The heterodyned signal along the reference beam was then defocused (L 7) onto the face of an RCA model 8645 photomultiplier (L 8) powered by a regulated high voltage supply (L 9) at, typically, 1600 V in a darkened room. The focusing lens, mounted on a vernier screw traverse, could be rapidly positioned by a drive motor (L 5) and its location relative to the cylindrical wall was determined with the aid of a Veeder Root counter (L 6). The relation between the lens position and the focal position within the cylinder had to be worked out with ray tracing techniques because of the relatively thick (about 1·2 cm) cylinder wall. These and other details concerning the probe volume, signal-to-noise ratio, etc., are available in the author's thesis (Weidman 1973).

2.5. *Doppler signal electronics*

Again referring to figure 1, the Doppler signal from the photomultiplier was monitored by a d.c. ammeter (D 1), and impedance matching to the recording electronics was provided by a field-effect transistor (D 2). The signal was then filtered (D 3), amplified (D 4), and observed on either an oscilloscope (D 5) or a spectrum analyser (D 6). Accurate frequency calibration of the spectrum analyser was made with a signal generator (D 7) and digital counter (D 8). Doppler frequencies, which could be readily measured with this set-up, ranged from 7 kHz to almost 1 MHz.

The signal processing system was relatively unsophisticated in that no Doppler-frequency tracker was employed. Synchronous velocity–time measurements were obtained by recording the observed Doppler frequency on the spectrum analyser and simultaneously depressing the 'zero-check' button on the $X-Y$ plotter to mark the time of measurement. When acceleration rates were too rapid, multiple runs were necessary to obtain a well-defined velocity profile.

3. Mean flow measurements

Most of the unsteady velocity measurements were taken at the three radial positions $r^*/a = 0{\cdot}334$, $0{\cdot}517$ and $0{\cdot}807$ in a plane approximately $\frac{1}{3}h$ from one end of the cylinder. The focal volume of the laser beams was positioned at a fixed radius and the average Doppler frequency was recorded at various times during spin-up or spin-down. In the presentation of data the velocities are non-dimensionalized with the maximum cylinder speed and plotted against the non-dimensional time $\bar{t} = t^*/t^*_w$, where $t^*_w = |(\Omega_i - \Omega_f)/\alpha|$ is the acceleration period of the cylinder. Also included in each figure is a typical velocity history of the cylindrical container as recorded on the $X-Y$ plotter.

The theoretical curves were computed using the average acceleration rate of all runs at a given radius. In table 1 we list the average Ekman numbers $E_\alpha = \nu/\surd\alpha^{\frac{1}{2}}h^2$ for the cases which necessitated multiple runs to obtain a well-defined velocity profile; the maximum percentage deviation from the average and the total number of runs are also tabulated. Initial and final angular velocities are not listed since they were always repeatable to better than 1 %. The parameters in the figure captions represent a simple average over all runs at all radii.

As a measure of how rapidly the cylinder is accelerated or decelerated, a comparison of the wall acceleration period t^*_w with the ordinary impulsive Ekman spin-up time $t^*_{\mathrm{EK}} = E_\Omega^{-\frac{1}{2}}\Omega^{-1}$ is made in figures 2, 4 and 6 by plotting the ratio $\bar{t}_{\mathrm{EK}} = t^*_{\mathrm{EK}}/t^*_w$. Note that this is the inverse of the abscissa in figure 11 of part 1.

3.1. *Nonlinear spin-up*

Measurements for spin-up from rest covering the Ekman numbers

$$E_\alpha = 2{\cdot}34 \times 10^{-6} \quad \text{to} \quad 27{\cdot}0 \times 10^{-6}$$

are given in figures 2(*a*)–(*c*). The final angular velocity in each case was approximately 110 rad/s. Interior solutions for $\bar{t} \leqslant 1$ were obtained by numerically integrating equation (I 3.11) for the characteristic paths using the full nonlinear expression (I 2.6) for $f(s)$; the solutions were continued into the post-acceleration

Figure number	r^*/a	Average $E_\alpha \times 10^6$	Maximum % deviation	Number of runs
2(*b*)	0·334	8·70	2·0	3
2(*b*)	0·517	8·71	2·5	6
2(*b*)	0·807	8·75	3·0	5
2(*c*)	0·334	2·36	2·0	7
2(*c*)	0·517	2·26	4·0	7
2(*c*)	0·807	2·36	3·0	9
4(*c*)	0·330	10·29	1·0	3
4(*c*)	0·514	10·33	1·5	4
4(*c*)	0·626	9·59	1·0	3
4(*c*)	0·727	9·56	0·7	3
4(*c*)	0·804	10·18	2·5	9
4(*c*)	0·850	9·75	1·0	3
4(*c*)	0·900	9·70	0·5	3
4(*c*)	0·925	9·82	1·0	3
4(*c*)	0·950	9·62	1·0	3
4(*c*)	0·975	10·48	1·5	3

TABLE 1. Experimental conditions for multiple runs in figures 2(*b*) and (*c*) and 4(*c*).

region $\bar{t} > 1$ with the aid of equation (I 3.4). The dotted lines indicate the double-valuedness of the inviscid interior solution at the wave front.

It seems appropriate to provide here a qualitative description of the spin-up process as derived from the flow-visualization study to be reported in § 4. When the cylinder begins to accelerate, distinct roll waves appear around the perimeter of the end wall, where the fluid is sheared. (These eddies have also been observed by McLeod 1922.) At the same time a strong cylindrical jet erupts from each end of the container and speeds axially along the curved wall towards the mid-plane. At low accelerations ($\alpha \simeq 0{\cdot}2\,\mathrm{rad/s^2}$) the turbulent jets recede back to the end walls before reaching the central plane, but at moderate accelerations

$$(\alpha \simeq 1{\cdot}0\,\mathrm{rad/s^2})$$

they coalesce to form a turbulent annular column adjacent to the curved wall; the column soon disappears in the reverse order in which it was formed, namely, it relaminarizes first near the mid-plane and then recedes back to the end plates. At still larger accelerations ($\alpha \gtrsim 4\,\mathrm{rad/s^2}$) the turbulent column thickens and then relaminarizes completely at the outermost radii as the fluid there spins up; thus we have the picture of a turbulent annular column of rotating fluid bounded on both sides by laminar flow. The turbulent column follows for a short while behind the wave front, but eventually disappears, leaving an entirely laminar approach to solid-body rotation.

Photographs of the end-wall flow patterns visualized with aluminium tracers are presented in figure 3 (plate 1). These prints correspond to successive times during spin-up from rest at the Ekman number $E_\alpha = 7{\cdot}64 \times 10^6$. Photograph (*a*) shows remnants of the initial roll waves, which have broken up and dispersed; the central core of undisturbed fluid can also be identified. In (*b*) the large eddies

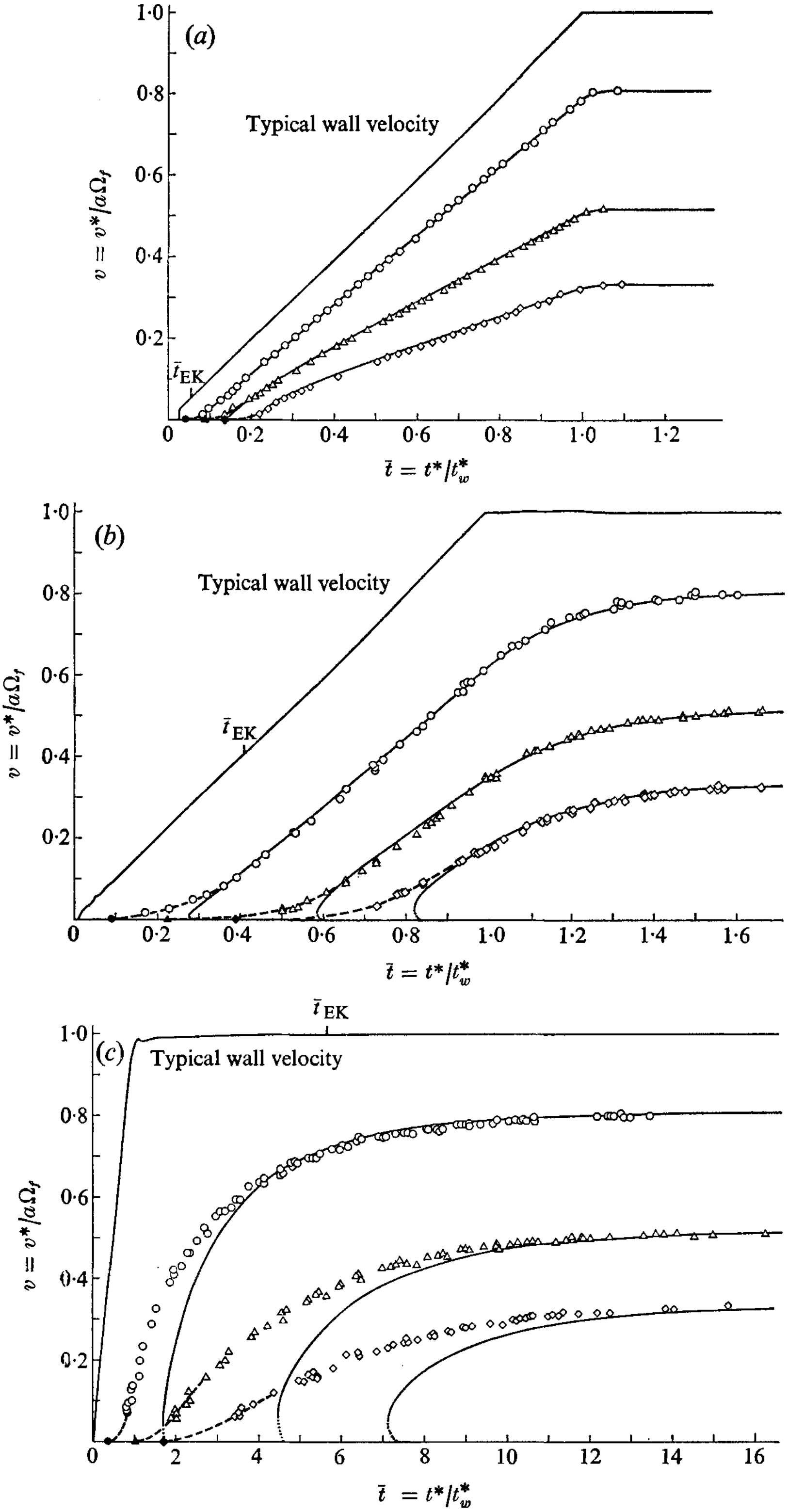

FIGURE 2. Spin-up from rest. ○, $r^*/a = 0{\cdot}807$; △, 0·517; ◇, 0·334; ——, interior solution; ●, ▲, ◆, wave-front flow-visualization data. (*a*) $E_\alpha = 27{\cdot}0 \times 10^{-6}$, $\Omega_f = 106{\cdot}6$ rad/s, $\alpha = 0{\cdot}209$ rad/s^2, $\bar{t}_{EK} = 0{\cdot}0541$. (*b*) $E_\alpha = 8{\cdot}74 \times 10^{-6}$, $\Omega_f = 108{\cdot}7$ rad/s, $\alpha = 1{\cdot}52$ rad/s^2, $\bar{t}_{EK} = 0{\cdot}409$. (*c*) $E_\alpha = 2{\cdot}34 \times 10^{-6}$, $\Omega_f = 108{\cdot}7$ rad/s, $\alpha = 21{\cdot}1$ rad/s^2, $\bar{t}_{EK} = 5{\cdot}68$.

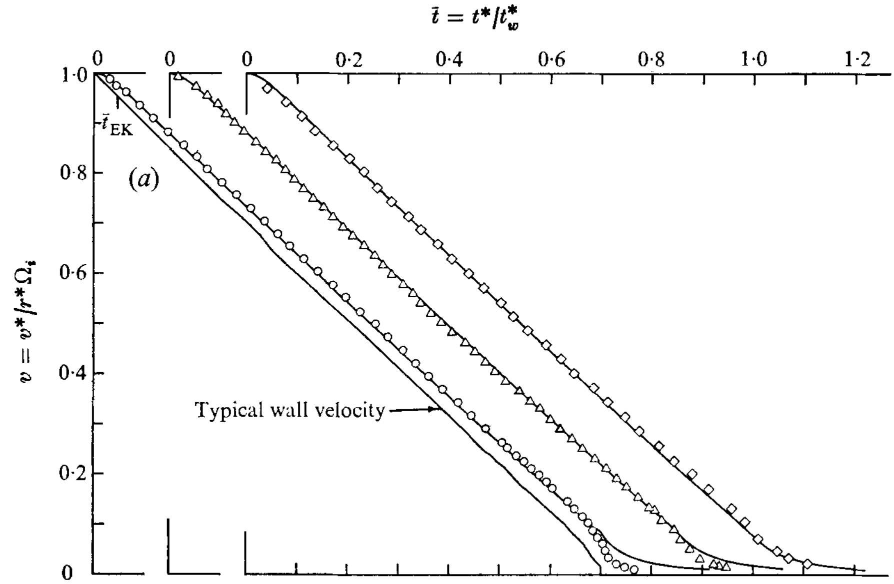

FIGURE 4(*a*). For legend see p. 718.

have disappeared and the first appearance of Ekman spiral waves can be discerned at large radii. In (*c*) a complicated pattern of bifurcating Ekman spirals has developed and the small quiescent core shows that virtually all the fluid has now begun to spin up. Photograph (*d*), taken just after the cylinder reached its steady-state velocity, exhibits symmetric Ekman spirals of almost constant wavelength, but these eventually disappear as the fluid catches up with the angular speed of the cylinder.

An estimate of the turbulent pumping in the Ekman layers was made by observing the duration and radial extent of the turbulent annulus. It is concluded that the flow was predominantly laminar for the two largest Ekman numbers, but at $E_\alpha = 2{\cdot}34 \times 10^{-6}$ the turbulent pumping may account for as much as 30 % of the total flux through the Ekman layers.

A measurement of the arrival time of the wave front at the three radial measurement stations was obtained from end-wall photographs similar to those in figure 3 taken at the various Ekman numbers. These data, plotted as zero velocity in figures 2(*a*)–(*c*), appear earlier than the first recorded velocities in each case. A discussion of this point is deferred to § 5.

3.2. *Nonlinear spin-down*

Measurements of spin-down to rest from $\Omega_i \simeq 110$ rad/s are plotted in figures 4(*a*)–(*c*). Only relatively slow decelerations covering the Ekman numbers $E_\alpha = 9{\cdot}92 \times 10^{-6}$ to $25{\cdot}4 \times 10^{-6}$ are presented since the flow was observed to become unstable rather quickly when the cylinder was spun down more rapidly. The interior solutions have been computed from (I 4.9) for $\bar{t} \leqslant 1$ and from (I 4.5) for $\bar{t} > 1$. The calculations in figures 4(*b*) and (*c*) are based on an average deceleration rate to rest, but in figure 4(*a*) the small impulsive stop was taken into

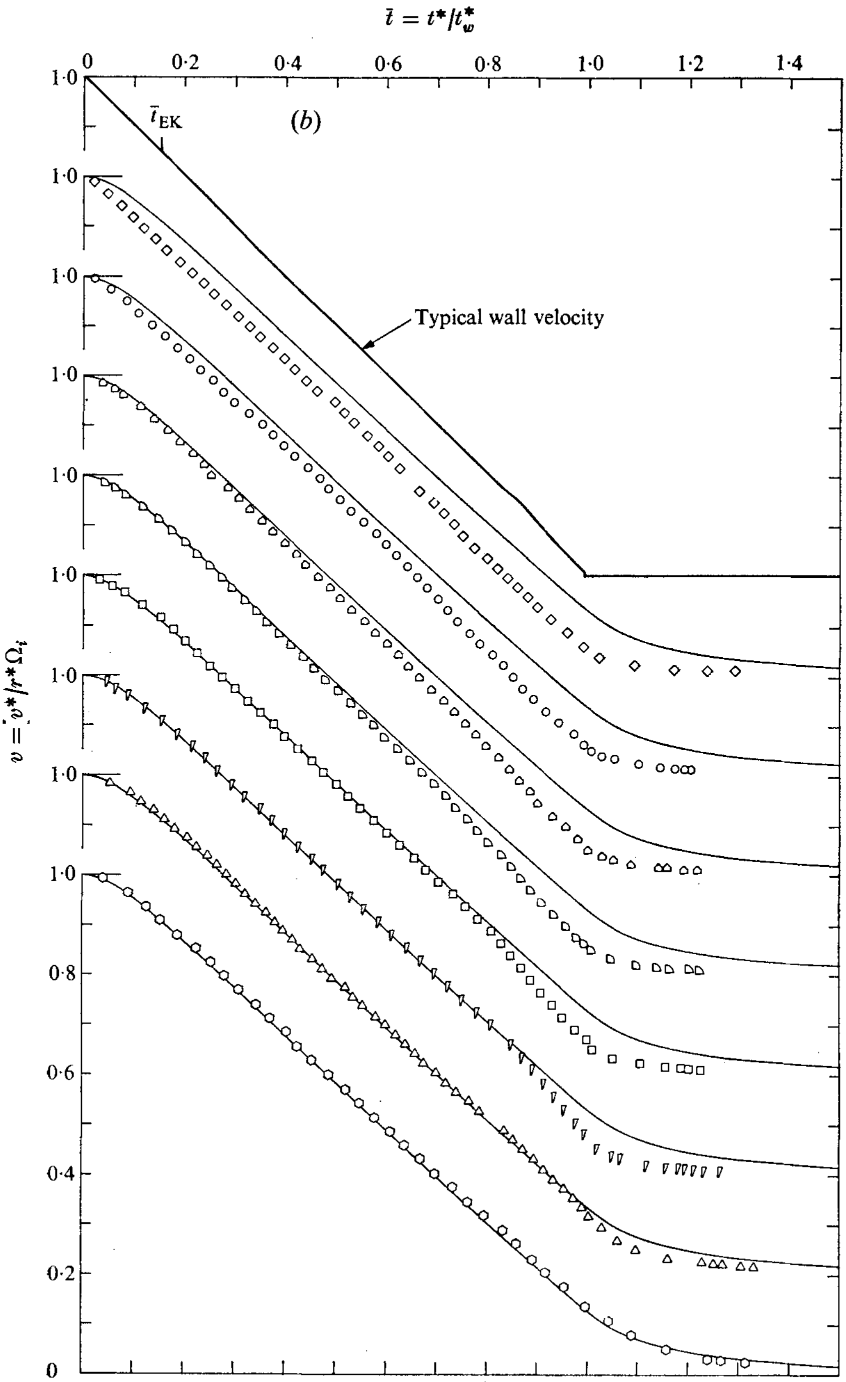

FIGURE 4(*b*). For legend see p. 718.

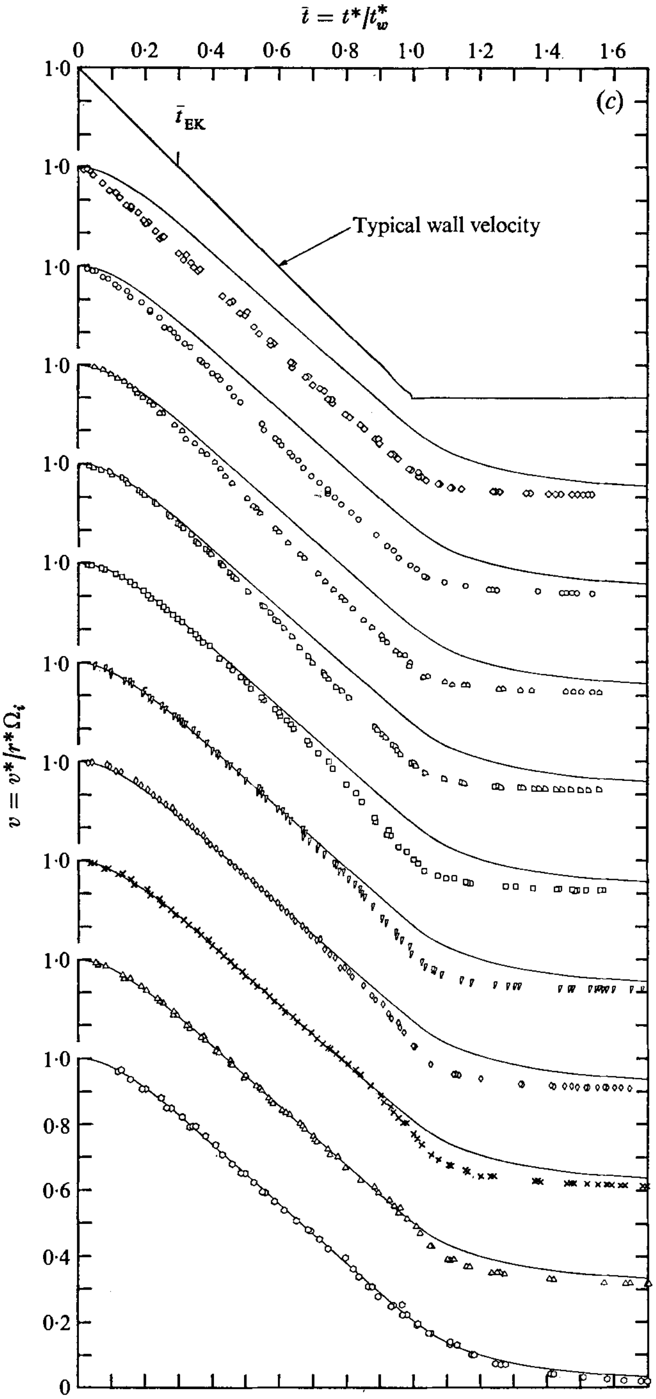

FIGURE 4. Spin-down to rest. ——, interior solution. (*a*) $E_\alpha = 25{\cdot}4 \times 10^{-6}$, $\Omega_i = 108{\cdot}3$ rad/s, $\alpha = -0{\cdot}179$ rad/s^2, $\bar{t}_{EK} = 0{\cdot}0485$; ○, $r^*/a = 0{\cdot}807$; △, 0·517; ◇, 0·334. (*b*) $E_\alpha = 13{\cdot}8 \times 10^{-6}$, $\Omega_i = 108{\cdot}9$ rad/s, $\alpha = -0{\cdot}535$ rad/s^2, $\bar{t}_{EK} = 0{\cdot}148$; ◇, $r^*/a = 0{\cdot}975$; ○, 0·950; ⌂, 0·925; ▱, 0·900; □, 0·850; ▽, 0·804; △, 0·514; ⬡, 0·330. (*c*) $E_\alpha = 9{\cdot}92 \times 10^{-6}$, $\Omega_i = 109{\cdot}0$ rad/s, $\alpha = -1{\cdot}083$ rad/s^2, $\bar{t}_{EK} = 0{\cdot}296$; ◇, $r^*/a = 0{\cdot}975$; ○, 0·950; ⌂, 0·925; ▱, 0·900; □, 0·850; ▽, 0·804; ◇, 0·727; ×, 0·626; △, 0·514; ⬡, 0·330.

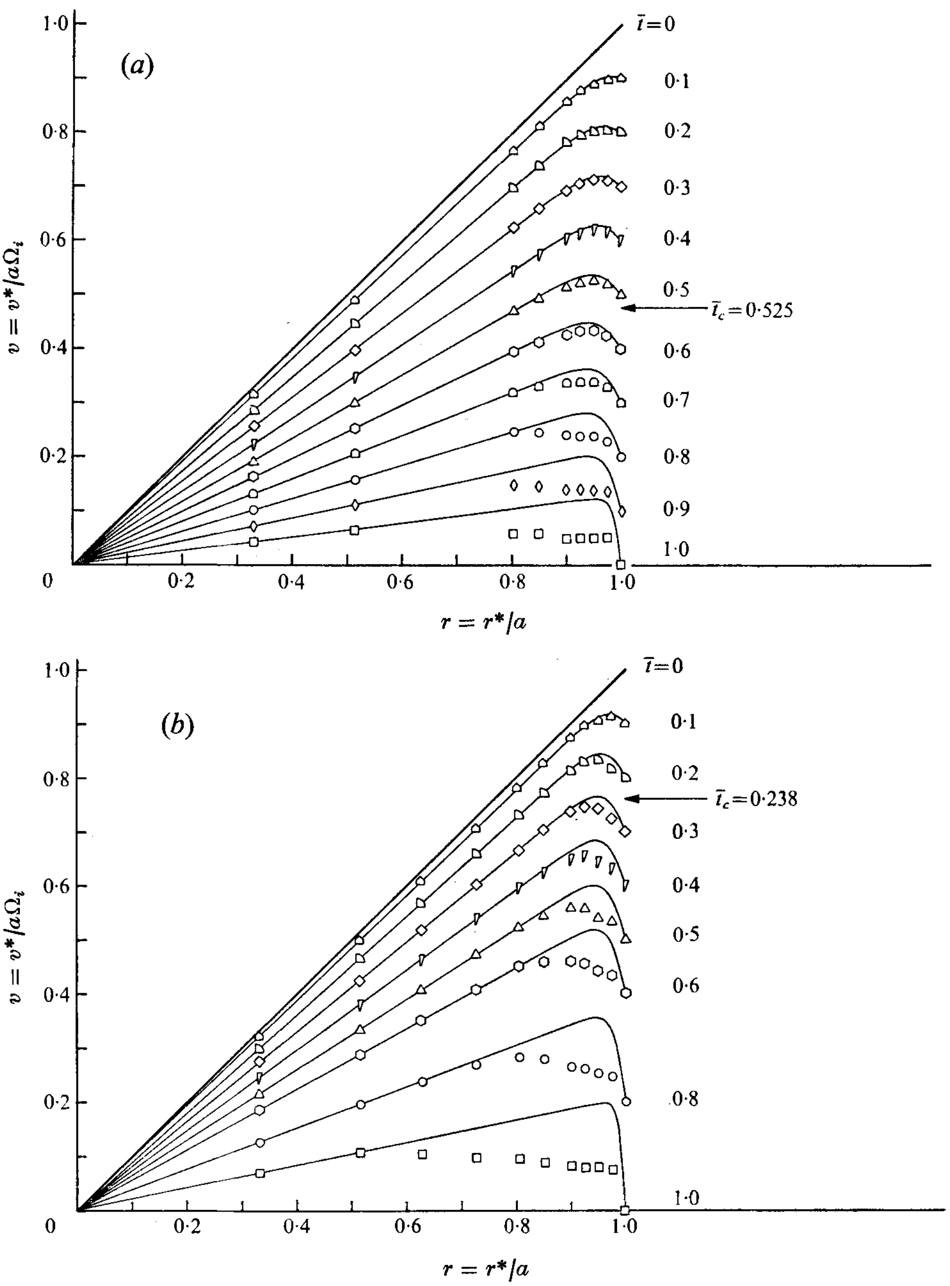

FIGURE 5. Boundary-layer profiles for spin-down to rest; $\bar{t}_c$ = time for instability as observed from flow visualizations. —, boundary-layer solution. (*a*) $E_\alpha = 13·8 \times 10^{-6}$, $\Omega_i = 108·9$ rad/s, $\alpha = -0·535$ rad/s², $\bar{t}_{EK} = 0·148$. (*b*) $E_\alpha = 9·92 \times 10^{-6}$, $\Omega_i = 109·0$ rad/s, $\alpha = -1·083$ rad/s², $\bar{t}_{EK} = 0·296$.

account; this is apparent in the small slope discontinuity in the velocity at $\bar{t} = 1$. The radial boundary-layer profiles, figures 5 (*a*) and (*b*), were obtained by cross-plotting the data in figures 4 (*b*) and (*c*) at selected times. The onset times $\bar{t}_c$ of the centrifugal instability, noted from the flow visualizations, are marked in figures 5 (*a*) and (*b*) and the theoretical velocity distributions are those obtained by numerical integration of (I 4.17).

3.3. *Linear spin-up and spin-down*

Measurements of small Rossby number flows at moderate accelerations from one non-zero angular velocity to another are presented in figures 6 (*a*) and (*b*). Corresponding theoretical results for spin-up (figure 6*a*) were obtained from the solutions in § 3.5 of part 1, using the value $k = 1{\cdot}02$ for the linearized suction in (I 2.8). A calculation of the terminal position of the dividing characteristic gives $(r_0)_f = 0{\cdot}613$; the shear discontinuity at the wave front (dividing characteristic) was so weak when it crossed $r^*/a = 0{\cdot}807$ that it cannot be discerned at its time of crossing, $\bar{t} = 0{\cdot}474$.

The linearized spin-down curves in figure 6 (*b*) were calculated from the Airy-function solution (I 4.11). The constant of proportionality for $g(\sigma)$ in (I 2.8) was $k = 1{\cdot}03$. We note that k was *not* chosen to obtain a best fit with the experimental results, but rather as a best fit to Rogers & Lance's Ekman-suction computations (cf. figure 1 of part 1) in the ranges $0{\cdot}8 \leqslant s \leqslant 1{\cdot}0$ and $0{\cdot}8 \leqslant \sigma \leqslant 1{\cdot}0$.

3.4. *Remarks about the measurements*

An analysis has shown that the expected *relative* errors for the frequency, time and position measurements are $\pm 0{\cdot}015$, $\pm 0{\cdot}005$ and $\pm 0{\cdot}010$ respectively. More scatter is evident in figures 2 (*b*) and (*c*) and 4 (*c*) owing to the slight non-repeatability of the multiple runs (see table 1). Also, since the measured speed curves for the cylinder were only linear to within $\frac{1}{2}$–3 %, the selection of an average acceleration rate introduces additional errors when comparing theory with experiment.

The reader is reminded that the measurements presented here are really mean flow data since they represent an average in both time and space. It is estimated that Doppler-frequency fluctuations greater than about 0·2 Hz could not be discerned, and hence the velocities constitute an average over as many as three cylinder revolutions at the highest rotational speeds. At low angular velocities, on the other hand, the Doppler signal could be resolved over just a fraction of a revolution of the fluid. No azimuthal asymmetries were apparent at these speeds, except in the final stages ($\bar{t} \gtrsim 1$) of spin-down to rest. Here, significant velocity excursions ($\Delta v/v \simeq 0{\cdot}15$) due to the breaking up of the regular Görtler cells were apparent; the plotted data for these cases represent an average of the observed low-frequency fluctuations.

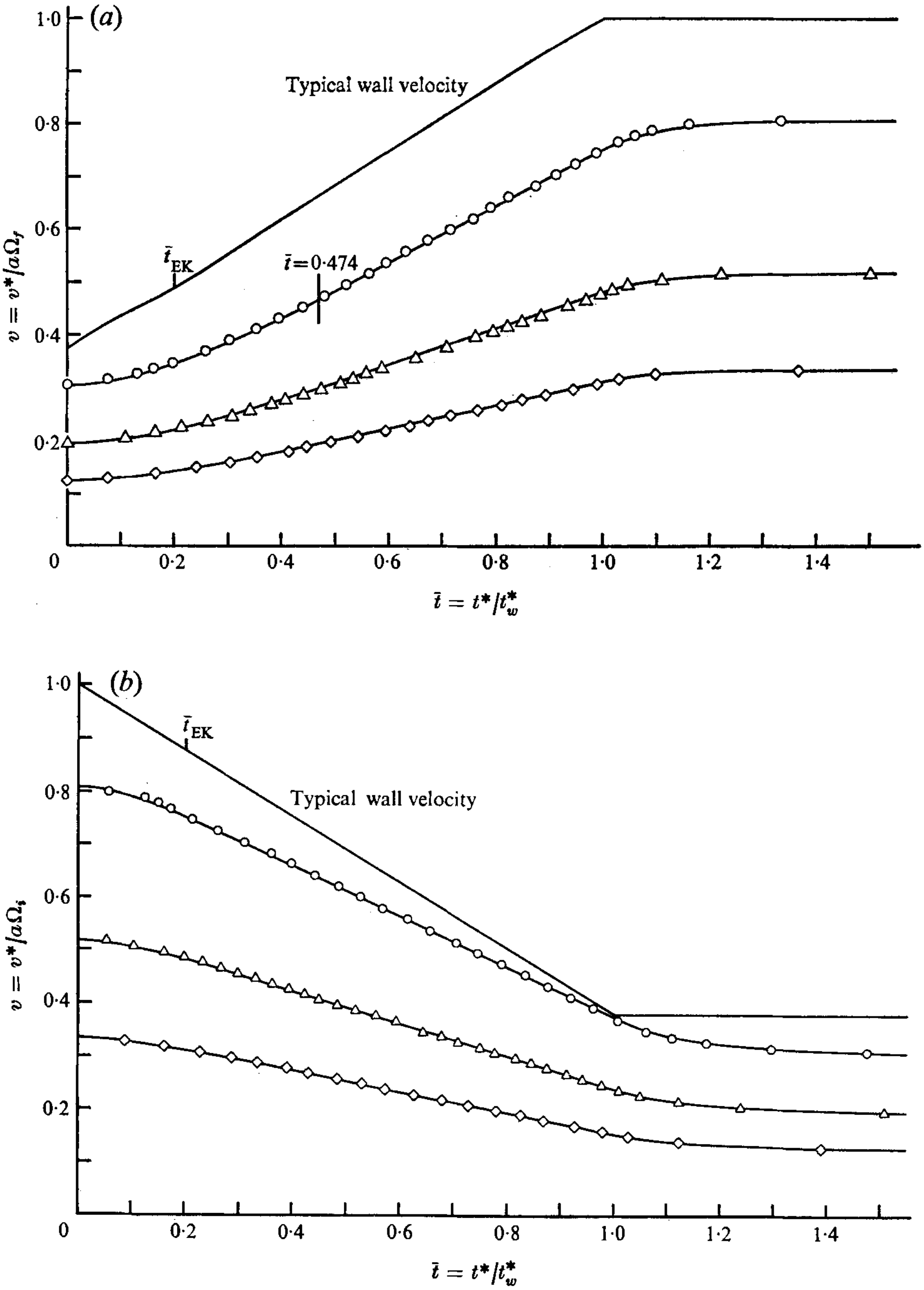

FIGURE 6. Small Rossby number flows. ○, $r^*/a = 0{\cdot}807$; △ 0·517; ◇, 0·334; ——, linearized interior solution. (*a*) Spin-up; $E_\alpha = 16{\cdot}2 \times 10^{-6}$, $\Omega_i = 39{\cdot}0$ rad/s, $\Omega_f = 104{\cdot}0$ rad/s, $\alpha = 0{\cdot}433$ rad/s^2, $\bar{t}_{EK} = 0{\cdot}200$, $\bar{t} = 0{\cdot}474$ is time of passage of wave front across station $r^*/a = 0{\cdot}807$ according to the interior solution. (*b*) Spin-down; $E_\alpha = 15{\cdot}8 \times 10^{-6}$, $\Omega_i = 104{\cdot}4$ rad/s, $\Omega_i = 39{\cdot}8$ rad/s, $\alpha = -0{\cdot}423$ rad/s^2, $\bar{t}_{EK} = 0{\cdot}200$.

4. Stability observations

Qualitative and quantitative observations of the fluid motion during spin-up and spin-down were made with the aluminium-tracer visualization technique; cf. Maxworthy (1971). With proper illumination, most of the spin-up and spin-down flow patterns, as well as their associated instabilities, could be readily observed.

The fluid transport along the cylinder's end walls during spin-up could always be visualized since the Ekman suction continuously entrained aluminium particles from the quiescent interior (region I), pumped them radially out through the boundary layers on the end plates, and eventually ejected them into the interior fluid behind the wave front (region II). As the fluid span up in region II, the heavier aluminium flakes were centrifuged to the cylindrical boundary, ultimately rendering the fluid transparent. The qualitative features of the spin-up motion have already been discussed in § 3.1. In the early stages of spin-down to rest, the interior motion could not be visualized because the aluminium adhered to the cylindrical boundary. Eventually, however, the centrifugal instability appeared and formed cellular motions which scoured the aluminium flakes off the wall. The tracers then found their way to the fluid interior by first travelling axially along the cylindrical wall, and then radially inwards through the Ekman layers.

Measurements of the stability boundaries for the Ekman and centrifugal instabilities observed in this experiment are presented in the following two sections.

4.1. *Ekman instabilities*

Documentation of the Ekman-spiral instabilities which attended spin-up was made in the following manner. High-speed photographs of the patterns on the cylinder's end plates were taken at 3 s intervals for accelerations closely duplicating the Ekman numbers of figures 2(*a*) and (*b*) and at 1 s intervals for the fastest acceleration, corresponding to figure 2(*c*). Close scrutiny of the sample photographs in figure 3 will reveal three black circles on the glass cover plate, corresponding to $r^*/a = 0{\cdot}334$, $0{\cdot}517$ and $0{\cdot}807$. From an analysis of the negatives one could determine whether a particular circle corresponded to an Ekman flow that was laminarly stable, laminarly unstable or (with some subjective judgment) turbulent. For example, in figure 3(*d*) the flow was noted to be laminarly stable at the inner circle and laminarly unstable at the two outer circles. If the flow around a given circle appeared to be only partially unstable (uncommon), or if the circle appeared as a demarcation between laminar flow and the laminar spiral waves, it was called 'marginally stable'. The measured velocity profiles were then used to compute the local Rossby number *Ro* and Reynolds number *Re*. In calculating these parameters we adhere to the definitions prevalent in the literature, namely,

$$Ro = \tfrac{1}{2}V_g/V_{\text{wall}} = (v^* - \Omega r^*)/2r^*\Omega, \quad Re = V_g\delta/\nu = |v^* - \Omega r^*|/(\nu\Omega)^{\frac{1}{2}},$$

where $V_g = v^* - \Omega r^*$ is the local geostrophic velocity and $\delta = (\nu/\Omega)^{\frac{1}{2}}$ is the thickness of the Ekman layer.

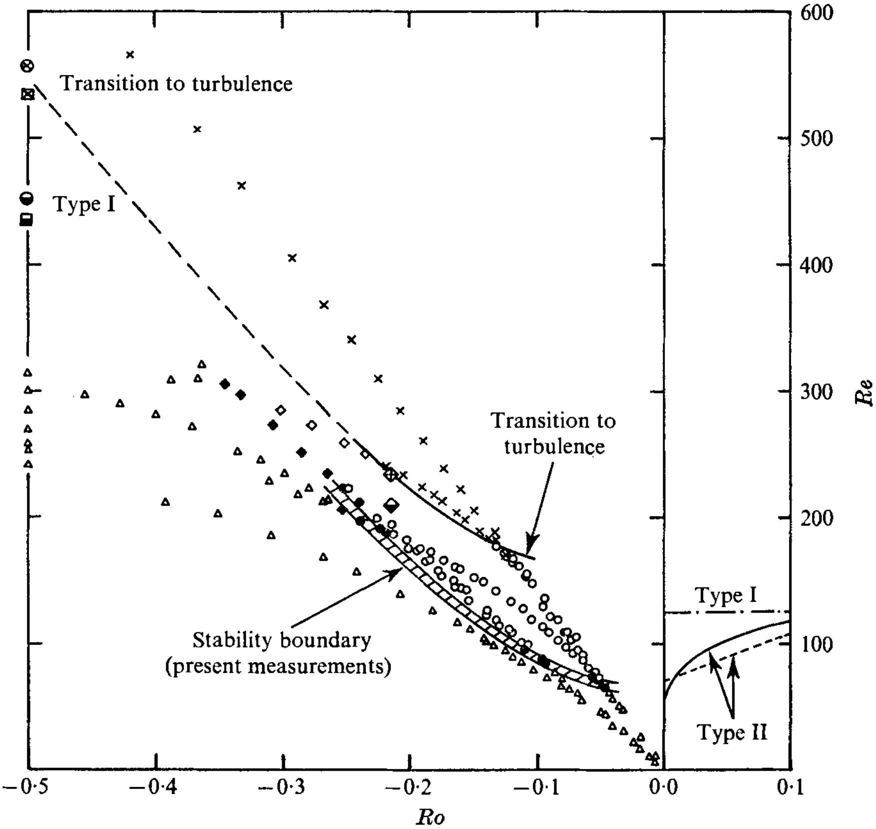

FIGURE 7. Observations of Ekman waves and transition to turbulence. △, laminarly stable; ×, turbulent. Group 1 (*Ro* > −0·25): ●, marginally stable; ○, laminarly unstable. Group 2 (*Ro* < −0·25): ◆, marginally stable; ◇, laminarly unstable. Comparison data for $(Re)_c$: —·—, Tatro & Mollo-Christensen (1967); ——, Caldwell & Van Atta (1970); - -, Faller & Kaylor (1965); ⊟, ⊠, Gregory *et al.* (1955); ⊖, ⊗, Smith (1947); ◈, type I waves; ⟡, type II waves, Faller & Kaylor (1965).

The stability measurements are summarized in figure 7. In order to help determine whether we are observing the almost stationary type I or rapidly moving type II waves, measurements of the average wavelength λ (band spacing normal to the wave fronts) and the angle of orientation ϕ with respect to the geostrophic flow were obtained. The data fall into two groups as indicated in figure 7. In the first group, for $Ro > -0{\cdot}25$, results from 69 measurements give an average wavelength $\lambda/\delta = 20{\cdot}4$ with a standard deviation of 2·4. The bands were all oriented to the right of the geostrophic flow at angles varying from 1 to 7°. The waves in the neighbourhood $-0{\cdot}20 < Ro < -0{\cdot}25$ often appeared in a bifurcating pattern. A listing of the measured wavelengths along the shaded stability boundary sketched in figure 7 shows no apparent trend with Rossby or Reynolds number (Weidman 1973). The few remaining measurements in the second group revealed a general decrease in wavelength from about $\lambda/\delta = 18$ near $Ro = -0{\cdot}25$ to $\lambda/\delta = 10$ at $Ro = -0{\cdot}35$ with band orientations still to the right of the geostrophic flow.

Reference	Wave type	R_0	$(Re)_c$	λ/δ	ϕ
Measurements					
Smith (1947)	I	−0·5	452	—	—
Gregory *et al.* (1955)	I	−0·5	436	21·5	14°
Faller (1963)	I	0·0	125 ± 5	10·9	14·5° ± 2°
Faller & Kaylor (1965)	II	$(Re)_c = 70 + 412\,Ro$		22 − 33	+ 5° to − 20°
Faller & Kaylor (1965)	I	−0·216	210	15	Positive
Faller & Kaylor (1965)	II	−0·216	234	38	Negative
Tatro & Mollo-Christensen (1967)	I	$(Re)_c = 124{\cdot}5 + 7{\cdot}32\,Ro$		11·8	14·6° ± 0·8°
Tatro & Mollo-Christensen (1967)	II†	$(Re)_c = 56{\cdot}3 + 116{\cdot}8\,Ro$		27·8 ± 2·0	0° to − 8°
Caldwell & Van Atta (1970)	II	0·0	56·7	—	—
Present data	II	0·0	60	20·4 ± 2·4	− 1° to − 7°
Theory					
Faller & Kaylor (1966)	I	0·0	118	11	10° to 12°
Faller & Kaylor (1966)	II	0·0	55	24	− 15°
Lilly (1966)	I	0·0	110	11·9	8°
Lilly (1966)	II	0·0	55	21	− 20°

† A recent study by Cerasoli (1975) suggests these waves were disturbances induced by the measurement probe.

TABLE 2. A summary of Ekman instability measurements and theory.

A summary of existing theoretical and experimental data on Ekman instabilities is provided in table 2. The angle of orientation ϕ is positive if the bands lie to the left of the geostrophic flow when viewed from *above* the Ekman layer. The critical Reynolds numbers, $(Re)_c$, for both wave types in table 2 are plotted in figure 7 for comparison with the present measurements. We have chosen not to plot Tatro & Mollo-Christensen's (1967) measurements reported as type II Ekman instabilities since there is strong evidence in the recent study by Cerasoli (1975) that these waves were probe-associated disturbances. Gregory *et al.* (1955) made a series of observations at $Ro = -0{\cdot}5$, and the Reynolds numbers given here for both the onset of type I waves and transition to turbulence represent an average of their data; also, the non-dimensional wavelength reported here for their type I waves was calculated by Faller (1963). The $(Re)_c$ measurements for type II waves reported by Caldwell & Van Atta (1970) include a correction for finite-amplitude effects proposed by Faller & Kaylor (1966).

Since the present measurements, as well as the negative Rossby number observations of Faller & Kaylor (1965), were made under unsteady flow conditions, it is of interest to determine when and if they can be compared with the steady-flow measurements of other investigators. Faller & Kaylor (1965) argue that, since the Ekman layer responds rapidly (in a time of order Ω^{-1}) to changes in the geostrophic flow, the motion should be relatively steady on the spin-up time scale (of order t^*_{EK}) appropriate for their experiment. What is not discussed is the time scale for the formation of the spiral instabilities, which depends on the amplification rates at given Re and Ro. Their own observations, however, help resolve this point: the measurements reported at $Ro = -0{\cdot}216$ for both the type I and type II waves were taken 1·32 revolutions after accelerating their tank from 0·624 rad/s to 1·100 rad/s, and so the instabilities can respond as fast as the Ekman boundary layer. In the present investigation the time scale for changes in the geostrophic flow ranged from $O(t^*_{\mathrm{EK}})$ for the almost-impulsive spin-up case to the much longer times $O(t^*_w)$ for the slower accelerations, and hence there is reason to believe that the flow was reasonably 'steady'. This contention is supported by the results: in figure 7 a fairly well-defined stability boundary results, even though the data were gathered over a wide range of acceleration rates. The observed scatter is attributed partly to the photographic method of data acquisition and partly to the inexact correspondence between the Ekman numbers of the photographs and those of the velocity measurements. Because of these qualifications, measurement errors of the order of 5–10 % are expected.

4.2. *Centrifugal instabilities*

Clear visualization of the centrifugal instability was made possible by directing a stroboscopic light along the axis of the cylinder and synchronizing it with the cylinder speed during spin-down. Initially the walls were dark owing to the coating of aluminium on the interior surface, but then alternating light and dark circumferential streaks indicating the erosion pattern of the vortical cells appeared after the onset of instability. At large, almost impulsive decelerations the instability was observed within a fraction of a second of the spin-down motion commencing. Discrete circles formed simultaneously (as near as could be determined) across the length of the cylinder, but they rapidly broke up into bifurcating patterns as the flow tried to adjust itself to a new, larger wavelength. The development of these types of instabilities beyond their initial stage is discussed by Maxworthy (1971). When the cylinder was spun down less rapidly the onset of instability occurred later, and at the slowest rates of deceleration ($|\alpha| < 0{\cdot}2\,\mathrm{rad/s^2}$) the flow appeared stable during well over half the deceleration phase. At these slow decelerations the instability was first observed at about a distance $\frac{1}{6}h$ in from the end walls, but it soon spread across the entire length of the cylinder. The streaks took the form of spiral bands curling outwards from the mid-plane at $z = 0$ with an ever increasing helical angle to the end walls at $z = \pm\frac{1}{2}\mathrm{h}$. Maximum helical angles (measured with respect to cross-sectional planes perpendicular to the z axis) of 15 to 20° were observed.

The elapsed time between the start of spin-down and the first appearance of the streaks was measured for a variety of deceleration rates. These measurements must give a late time for instability, primarily because it takes a finite time for the amplification rates of a given wavelength to become large enough to scour away the aluminium particles which were centrifuged to the cylinder wall. Since it is difficult to estimate the correction due to this effect, we simply present the stability boundary as observed. In figure 8 the ordinate is the critical Görtler stability parameter, defined as $(G_\theta)_c = R_\theta(\theta/a)^{\frac{1}{2}} = (\omega^*_I - \Omega)\,\theta^{\frac{3}{2}}a^{\frac{1}{2}}/\nu$. R_θ is the Reynolds number based on the momentum thickness θ, which is calculated from the equation

$$\theta a^2(\omega^*_I - \Omega)^2 = \int_0^a (\omega^* - \Omega)\,(\omega^*_I - \omega^*)\,(r^*)^2\,dr^*,$$

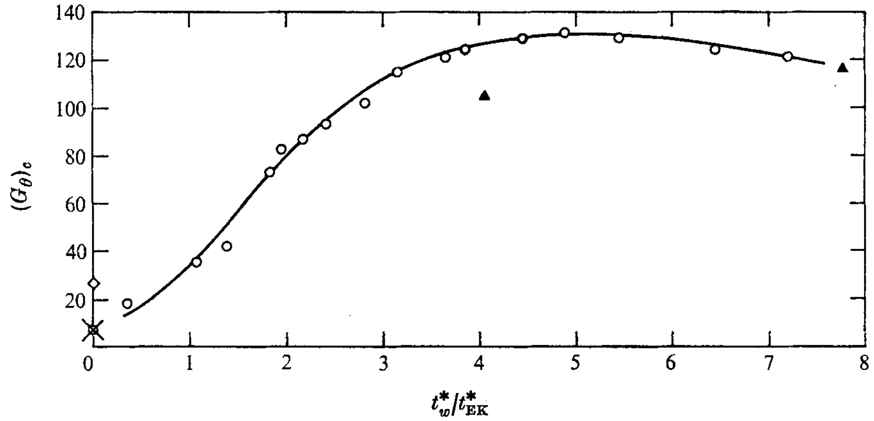

FIGURE 8. Observations of centrifugal instability during spin-down. ○, instability according to flow visualizations; ▲, instability deduced from the velocity profiles. Comparison data: □, Tillmann (1967); ◇, Maxworthy (1971); ×, Maxworthy with momentum-thickness correction.

where Ω is the instantaneous angular speed of the cylinder and ω_I^* and ω^* are computed from (I 4.17). Measurements by Tillmann (1967) and Maxworthy (1971) for impulsive spin-down to rest are included in figure 8, as well as a correction† to Maxworthy's original data. An extrapolation of the present results to $t_w^*/t_{EK}^* = 0$ seems to corroborate the more precise measurements of Tillmann and Maxworthy (with correction).

In figures 5(*a*) and (*b*) we see that, indeed, the visualization data do give a late time, since a comparison of the theoretical and experimental velocity profiles suggests that instability has already occurred at $\bar{t} \simeq 0{\cdot}45$ for $E_\alpha = 13{\cdot}8 \times 10^{-6}$ and at $\bar{t} \simeq 0{\cdot}15$ for $E_\alpha = 9{\cdot}92 \times 10^{-6}$. The critical Gortler stability parameter for these times, also plotted in figure 8, gives an indication of the error in the flow visualization data. In any case, both methods for determining the onset of instability suggest that the effect of decelerating the cylinder at a finite rate is to increase the critical stability parameter above its value for impulsive spin-down.

5. Discussion of results

It is clear that the unsteady fluid motion driven by a spinning cylinder at low Ekman numbers is inevitably complicated by flow instabilities which originate at the solid boundaries. Laminar spin-up is better behaved than spin-down because the motion is always centrifugally stable and because the Ekman instabilities, confined to thin layers adjacent to the top and bottom of the cylinder, do not measurably disrupt the interior flow. In § 5.1 we compare experimental

---

† The correction arises because Maxworthy (1971) assumed a Rayleigh boundary layer for the early development near the wall. Tillmann (1967), from an analysis due to Grohne, has shown that the small time development of the momentum thickness in an impulsively spun-down cylinder is $2^{\frac{1}{2}} - 1$ times smaller than for a Rayleigh boundary layer. The correction $(0{\cdot}414)^{\frac{3}{2}}$ applied to Maxworthy's measurements gives excellent agreement with Tillmann's data.

and theoretical velocity profiles as affected by these instabilities, and in § 5.2 the scaling of the vertical shear layers is considered in detail. The results of the stability observations are discussed in the remaining two sections.

5.1. *Mean interior flow*

In order to interpret the flow-visualization measurements for the arrival of the wave front, one must realize that the tiny aluminium tracers respond to very weak shearing motions (Maxworthy 1971). In the appendix, a model for the response of aluminium flakes to a propagating shear front is presented; the results suggest that the non-dimensional azimuthal velocity v and its time derivative $dv/d\bar{t}$ are of the orders 10^{-4} and 10^{-3} respectively when the aluminium disks begin to rotate under the shearing motion. Consequently, these data (solid symbols) at the three measurement stations have been plotted as zero velocity in figures 2 (*a*)–(*c*). Furthermore, under the assumption that $dv/d\bar{t}$ is negligibly small at these points, one can sketch in the missing velocity profiles at the viscous front; these are the dashed curves in the spin-up figures.

Let us consider now the measurements for spin-up from rest. It has been shown by plotting that the agreement between the experiment and the theoretical profiles in figures 2 (*a*)–(*c*) is much better than could have been obtained using a linear expression for the Ekman suction, so the flow is truly nonlinear for $\Delta\Omega/\Omega = 1$. At lower Rossby numbers ($0{\cdot}26 \leqslant \Delta\Omega/\Omega \leqslant 0{\cdot}58$), Ingersoll & Venezian (1968) demonstrated that a linear Ekman-suction model adequately predicts the spin-up motion away from the wave front, but they found that the proportionality constant depends on the Rossby number. This result is easily explained in terms of Rogers & Lance's Ekman-suction curve (figure 1, part1); clearly, a linear fit in the range $1{\cdot}0 \geqslant \Delta\Omega/\Omega \geqslant 0{\cdot}2$ gives a reasonable approximation to the Ekman flux, but the optimum constant of proportionality varies with $\Delta\Omega/\Omega$.

Although the problem of the velocity discontinuity in the inviscid solution has not been resolved, the experimental data in figures 2 (*a*) and (*b*) show that its effect is felt only locally at the wave front in the form of a viscous tongue jutting ahead of the inviscid profile. After the passage of the tongue, the interior fluid spins up in almost exact agreement with the theoretical predictions for these accelerations where $t_w^*/t_{\mathrm{EK}}^* > 1$. In figure 2 (*c*), where $t_w^*/t_{\mathrm{EK}}^* < 1$ and the flow is nearly one of impulsive spin-up, the experimental data depart significantly from the theory over a major portion of the time. It is difficult to estimate the effect of the observed turbulent mixing for this case, but it is doubtful whether it could account entirely for the large discrepancy between theory and experiment. The sizable velocity discontinuity suggested by the inviscid solution shows the need for a more rigorous analysis of the inviscid equation at the wave front (e.g. a shock-fitted solution), or a computed integration of the full viscous equation before rejecting the Wedemeyer model at these large acceleration rates.

In spite of the fact that the details of the wave front are seen to vary considerably with E_α, the interior solution is always in good agreement with the experimental measurements during the final stages of spin-up. Thus the radially dependent spin-up times t^*_{99} presented in figure 11 of part 1, and computed for the present experimental conditions ($E_\Omega = 9{\cdot}3\times10^{-8}$), still provide a good measure of the global spin-up time.

The spin-down data in figures 4(*a*)–(*c*) cover a range of decelerations for which $t^*_w/t^*_{\mathrm{EK}} > 1$. The difference between the inviscid theory and experiment near $r^*/a = 1$ in figures 4(*b*) and (*c*) is shown in figures 5(*a*) and (*b*) to be due to the side-wall boundary layer when $\bar{t} < \bar{t}_c$ and due to the centrifugal instability at later times. The good agreement prior to the observed onset of instability vindicates *a posteriori* the 'quasi-steady' assumption made in the theoretical computation. The effect of the instability is to decelerate the fluid more rapidly by extracting energy from the mean flow. This is particularly evident at late times in figures 5(*a*) and (*b*), when the cells become large and extend well into the fluid interior. The flow at the innermost radial station remains virtually unaffected by disturbances from the side wall as far as the measurements were taken in figures 4(*a*)–(*c*), even during the late post-deceleration phase; the agreement between theory and experiment in this region confirms the algebraic decay predicted in part 1.

The close correspondence between theory and measurement for the linear flows in figures 6(*a*) and (*b*) provides a good example of the accuracy made possible with laser-Doppler velocimetry when the flow is laminar and stable. One might wonder about the effect of the centrifugal instability during spin-down, when in fact the flow-visualization measurements for the onset time $\bar{t}_c$ show that the vortical cells should have appeared before the end of the deceleration phase. Clearly, the measurements in figure 6(*b*) indicate that the flow was restabilized before any finite-amplitude effects could be discerned in the velocity profile at the nearest radial station $r^*/a = 0{\cdot}807$.

5.2. *Scaling of the vertical shear layers*

Venezian (1970) has shown that the shear discontinuity at the wave front given by Wedemeyer's (1964) analysis is smoothed out in a viscous layer $O(hE^{\frac{1}{4}}_\Omega)$ as long as $AE^{\frac{1}{4}}_\Omega \ll 1$. Indeed any viscous adjustment of the azimuthal velocity according to equation (I 3.6) must occur in a layer of this size since the viscous terms on the right-hand side only become important when $\partial/\partial r \sim (AE^{\frac{1}{4}}_\Omega)^{-1}$ for small E_Ω. Consequently, the shear-layer thickness δ_s must scale according to the relation

$$\delta_s/a \propto AE^{\frac{1}{4}}_\Omega \tag{5.1}$$

for both spin-up and spin-down. Watkins & Hussey (1976) report that according to (I 3.6) the transition from a purely convective time scale to a viscous time scale begins near $A^2E^{\frac{1}{2}}_\Omega = 0{\cdot}02$, and hence the scaling given by (5.1) can only be expected when $AE^{\frac{1}{4}}_\Omega < 0{\cdot}14$.

Values of δ_s have been estimated from sketches of the radial velocity profiles at various times $\bar{t}$ and are plotted against $AE^{\frac{1}{4}}_\Omega$ in figure 9. The Ekman numbers were calculated from the instantaneous angular speed of the cylinder, i.e. $E_\Omega = \nu/h^2\Omega(\bar{t})$. Open symbols correspond to the free shear layer in spin-up, closed symbols to the boundary layer in spin-down, and the dots relate to shear-layer estimates taken from the numerical calculations of Watkins &

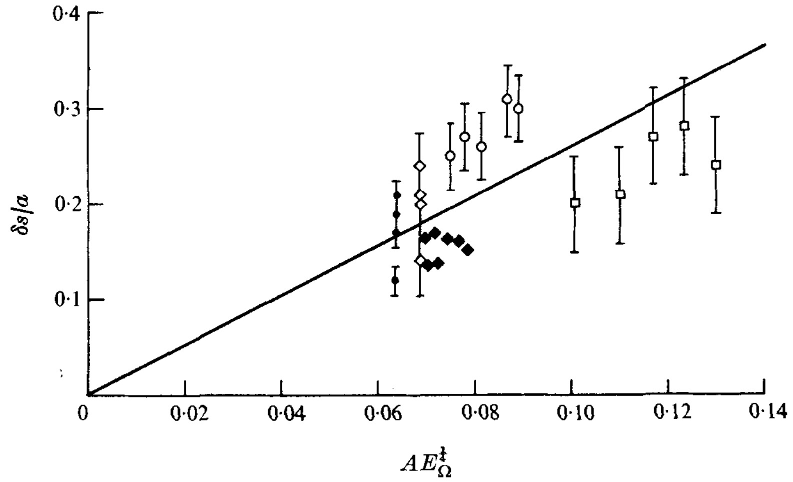

FIGURE 9. Estimates of vertical shear-layer thickness. ○, ◇, □, free shear layer in spin-up at constant acceleration, present experiments; ◆, side-wall shear layer in spin-down at constant deceleration, present experiments; ●, free shear layer in impulsive spin-up, from calculation of Watkins & Hussey (1976).

Hussey (1976). Error bars indicating the uncertainty in the estimates of δ_s according to the definitions listed below are included when necessary.

In the radial-velocity profiles sketched from the spin-up data in figures 2(*a*) and (*b*), δ_s was measured as the distance over which the true viscous front rose from zero velocity and merged with the inviscid profile. Only profiles for $\bar{t} > 1$ could be obtained from the data in figure 2(*c*), and here δ_s was taken to be the distance in which the velocity rose to $0{\cdot}1\, a\Omega_f$, since this was the region where the viscous tongue merged with the steep interior profile.

Radial-velocity distributions plotted from the four angular-velocity profiles given in figure 5 of Watkins & Hussey (1976) showed that the curvature went to zero (or changed sign) where the viscous front departed from the inviscid profile, hence estimates of δ_s were easily obtained. These profiles, as well as those obtained from the experimental data, exhibited only a slight steepening at the wave front. Estimates of the shear-layer thickness were not made for the remaining distributions presented by Watkins & Hussey because they fell outside the range $AE_\Omega^{\frac{1}{4}} < 0{\cdot}14$.

Boundary-layer thicknesses for spin-down were calculated from the theoretical velocity distribution in figures 5(*a*) and (*b*) at times prior to the observed instability, when theory and experiment were in substantial agreement. Here δ_s was measured from the wall to the point in the interior at which $\omega - r_1 = 0{\cdot}99 \times (\omega_I - r_1)$; this is essentially the point where the curvature in the velocity profiles drops to zero.

Some dependence of δ_s on the acceleration rate α is expected as well as some differences between spin-up and spin-down. Nevertheless, the results collected in figure 9 are all of similar order and offer good evidence for the scaling suggested by (5.1). The line drawn through the data has a slope of 2·6.

5.3. *Ekman instabilities*

The Ekman-boundary-layer instabilities for $Ro > -0{\cdot}25$ in figure 7 are characteristic of type II waves. The wave angle orientations, for example, are always negative in agreement with theoretical calculations, although we see from table 2 that Faller & Kaylor (1965) have observed type II waves at positive ϕ. The average wavelength $\lambda/\delta = 20{\cdot}4$ measured here is somewhat smaller than both the measurements and theoretical calculations reported by Faller & Kaylor in table 2, but there is close agreement with the numerical calculations of Lilly (1966). An extrapolation of the shaded stability boundary in figure 7 gives a zero Rossby number intercept near $(Re)_c = 60$, in good agreement with the theoretical predictions $(Re)_c = 55$ as well as the experimental estimates $(Re)_c = 70$ and $(Re)_c = 56{\cdot}7$ reported by Faller & Kaylor (1965) and Caldwell & Van Atta (1970), respectively.

Although there is strong evidence that the instabilities observed for $Ro > -0{\cdot}25$ are of the type II mode, it is less obvious what is happening at larger negative Rossby numbers. Faller & Kaylor (1965) measure onset of type II waves where transition to turbulence is noted in the present study, and their critical Reynolds number for type I waves is close to the type II stability boundary measured here. Progressing towards more negative values of Ro the band spacing decreases to values which might be typical for type I waves, but the bands are still oriented to the right of the geostrophic flow. Some of the discrepancies between the present measurements and those of Faller & Kaylor (1965) may be due to experimental error in the present data or real differences between the two experimental flows or both causes, but in either case there is no problem of probe-induced instabilities. Carefully controlled experiments of sufficient accuracy will be necessary to straighten out these discrepancies.

One can speculate as to why the type I waves are not observed when, judging from the ample theoretical and experimental information available at zero Rossby number, one would expect them to appear (at least for small negative Ro) at some Reynolds number between the type II stability boundary and the curve indicating the onset of turbulence in figure 7. It may be that visualizations with the opaque aluminium particles viewed through the bottom surface favour a particular mode of instability. In fact, the theoretical studies of Faller & Kaylor (1966) and also Lilly (1966) show that of the two wave modes the type II vortical rolls are the ones centred closest to the solid boundary.

The liberty was taken of extending the curve defining the onset of turbulence to the measured values reported by Smith (1947) and Gregory *et al.* (1955) at $Ro = -0{\cdot}5$. In the region of small positive Rossby number ($Ro \simeq 0{\cdot}15$), Caldwell & Van Atta (1970) note a transition to turbulence at $Re = 148$, while Tatro & Mollo-Christensen report a value above $Re = 200$. An extrapolation of the present data compares more favourably with the former investigators, but the transition Reynolds number may depend appreciably on the test facility and other factors which have not been experimentally controlled.

The data in figure 8 show the curious result that, when the cylinder is spun down at a finite rate, the critical Gortler stability parameter increases significantly above the values measured by Tillmann (1967) and Maxworthy (1971) for impulsive spin-down to rest. We note that the measurements of the latter investigators indicate finite amplitude instability since the computations by Hammerlin (1955) and Smith (1955), both representing improvements over Görtler's (1940) original calculations, give a minimum value $(G_\theta)_c = 0{\cdot}3$ for neutral stability. Likewise, the present measurements represent similar finite-amplitude observations, although the instability times noted from the aluminium-particle visualizations are undoubtedly somewhat later than would have been obtained with neutrally buoyant particles. The apparent agreement between the present measurements extrapolated to $t_w^*/t_{\mathrm{EK}}^* = 0$ and those of Tillmann and Maxworthy suggests that a unique value of the Görtler stability parameter ($(G_\theta)_c \simeq 6{\cdot}5$) is sufficient to predict 'finite amplitude' instability for impulsive spin-down to rest; a possible explanation for why this value does not also apply when the cylinder is spun down at a finite deceleration is given in the following paragraph.

The circular patterns observed at instability for nearly impulsive spin-down in the present experiment showed that the ratio of the axial velocity to the azimuthal velocity relative to the wall was small; in this respect the experiment corresponded to one-dimensional flow over a concave wall and the criterion for instability would be qualitatively that originally given by Görtler (1940). Furthermore, the onset of instability would be independent of the axial coordinate as noted in the present experiment. The observation of helical bands for the slow decelerations, on the other hand, indicates that the flow adjacent to the wall was substantially two-dimensional; in this case the stability criterion due to Ludweig for spiralling motions would be more appropriate. Ludwieg's (1964) stability boundaries calculated for viscous flow with helical streamlines can be used to show how the onset of instability might first occur at a particular axial station away from the mid-plane as observed in the present experiment. Moreover, although Ludwieg's results do not directly explain the increased magnitude of $(G_\theta)_c$ for the spiralling flow, there is no reason to believe it should not change since the instability is of a different type. The mechanism for instability may be somewhat more complicated than indicated above because the actual flow is known to be three-dimensional, but Ludwieg's (1964) stability analysis accounts for one observed feature not otherwise explained.

6. Summary and conclusions

Temporal velocity distributions for spin-up and spin-down at constant acceleration have been obtained using laser-Doppler anemometry. These measurements along with the calculated spin-up time scales given in figure 11 of part 1 suggest that the transient motion can be classed as either 'driven' for the relatively slow accelerations or 'impulsive' for the rapid accelerations, with transition occurring when $t_w^*/t_{\mathrm{EK}}^* = O(1)$. These flows are accompanied by time-dependent vertical shear layers which scale, approximately, with the instantaneous value of $AE_{\Omega}^{\frac{1}{4}}$ as long as $AE_{\Omega}^{\frac{1}{4}} < 0{\cdot}14$. In nonlinear spin-up the shear layer propagates away from the cylindrical wall, but in spin-down it remains attached as a boundary layer and provides the setting for centrifugal instability.

A comparison of the extended Wedemeyer theory with experiment for impulsive-like flows when $t_w^*/t_{\mathrm{EK}}^* < O(1)$ is tenuous at best. The strong centrifugal instability which soon engulfs the interior fluid motion precludes any possible evaluation of the spin-down theory in this parameter range. For the case of nearly impulsive spin-up the appreciable velocity discontinuity suggested by the numerical calculations shows the need for a more rigorous analysis of the inviscid Wedemeyer equation when accelerations are large. The measurements clearly deviate from the present (incomplete) inviscid computations for the flow near the wave front if one assumes that the observed turbulent shear column had negligible influence on the real flow. Further experiments are called for to obtain data at low enough Ekman numbers for the theory to be valid, but not so low that the flow becomes turbulent.

The measured velocities for the relatively slow accelerations when $t_w^*/t_{\mathrm{EK}}^* > O(1)$, however, nicely corroborate the generalized Wedemeyer theory for both linear and nonlinear flows away from the propagating shear layer in spin-up and outside the region of instability in spin-down. In particular, the 'quasi-steady' theory describing the side-wall boundary layer for spin-down as well as the algebraic decay to rest are confirmed experimentally. The centrifugal instability has a direct influence on the interior flow which results in a more rapid spin-down in regions affected. The Ekman instabilities observed during spin-up, on the other hand, play a passive role since they do not measurably disrupt the unsteady geostrophic flow. The propagating shear layer is seen to affect the spin-up motion only locally, and hence can be considered as simply an interesting detail of the flow when the wall acceleration period is sufficiently long. Moreover, the detailed azimuthal velocity distribution at the wave front may be contained in the viscous Wedemeyer equation, but one must be willing to carry out the tedious integrations necessary to extract this information.

The stability boundary in the *Re*, *Ro* plane for the spiral waves observed during spin-up has been determined from flow visualizations made using aluminium-particle tracers. For $Ro > -0{\cdot}25$ the instabilities are evidently of the type II Ekman mode since the waves are oriented to the right of the geostrophic flow, have an average wavelength $\lambda/\delta = 20{\cdot}4$ and a critical Reynolds number near 60 at $Ro = 0$, in substantial agreement with the results of other investigators listed in table 2. As with the measurements for positive *Ro* of Faller & Kaylor (1965) and Caldwell & Van Atta (1970) sketched in figure 7, the critical Reynolds number for the present experiment has a strong Rossby-number dependence, increasing monotonically away from the $Ro = 0$ axis. It is likely that the curve marking transition to turbulence will follow a similar rising trend from $Ro = 0$ to $Ro = -0{\cdot}5$.

Measurements of the onset of the centrifugal instability in spin-down have also been obtained and compared with the data of Tillmann (1967) and Maxworthy (1971) via the Görtler stability parameter. The results suggest that the critical

Görtler parameter for finite-amplitude instability is a function of the deceleration rate for spin-down in a cylinder. The observed features of the flow near the boundary at the time of instability show that it changes from being a basically one-dimensional circular flow for almost impulsive decelerations to a two-dimensional spiralling flow at the slower decelerations. Thus it is argued that the critical Görtler stability parameter need not necessarily remain constant since the instability changes qualitatively from that described by Görtler (1940) to that described by Ludwieg (1964).

The author is indebted to Tony Maxworthy for his guidance throughout the course of this work and also for his valuable comments in the writing of the manuscript. The author is grateful to Professor H. P. Greenspan for providing the unpublished theoretical results given in the appendix. Finally, particular thanks are given to Moritz Flink for constructing most of the experimental apparatus and Al Bleeker for his patient assistance during the long hours of data acquisition. This work was supported by the National Science Foundation under Grant GK 19107.

Appendix

The following model† is used to obtain an order-of-magnitude estimate of v and $dv/d\bar{t}$ at the time the aluminium flakes begin to respond to an oncoming shear flow. We consider the simplified one-dimensional Wedemeyer equation for impulsive spin-up including the effects of viscosity. This leads to a form of Burgers' equation

$$\frac{\partial v}{\partial \tau}+(1-v)\frac{\partial v}{\partial x} = E_{\Omega}^{\frac{1}{2}}\frac{\partial^2 v}{\partial x^2} \qquad \text{(A 1)}$$

for the shear velocity. Here $\tau = E_{\Omega}^{\frac{1}{2}}\,\Omega t^*$, $v = v^*/v_0$ and $x = x^*/h$ where v_0 is the velocity of the wall imparting the vorticity to the fluid and $E_{\Omega} = \nu/\Omega h^2$. The solution for (A 1) satisfying the boundary conditions $v(x,0) = 0$ and $v(0,\tau) = 1$ is given by

$$v(x,\tau) = \operatorname{erfc}(\eta)/[\operatorname{erfc}(\eta)+\exp(-x/E_{\Omega}^{\frac{1}{2}})\operatorname{erfc}(\xi)], \qquad \text{(A 2)}$$

with

$$\eta = \frac{\tau+x}{2E_{\Omega}^{\frac{1}{4}}\tau^{\frac{1}{2}}}, \quad \xi = \frac{\tau-x}{2E_{\Omega}^{\frac{1}{4}}\tau^{\frac{1}{2}}}.$$

We idealize the aluminium flakes to be perfect flat disks. Then, according to Jeffery (1922), the angle ϕ made by a disk in a vertical plane with the shear flow is given by

$$\cot\phi = -E_{\Omega}^{-\frac{1}{2}}\int_0^{\tau}\frac{dv}{dx}(x,\tau')\,d\tau'. \qquad \text{(A 3)}$$

(Jeffery's analytical results have been confirmed experimentally by Goldsmith & Mason (1962) for disks rotating in a flow of constant shear.)

---

† The author is indebted to Professor H. P. Greenspan (private communication) for providing these unpublished theoretical results.

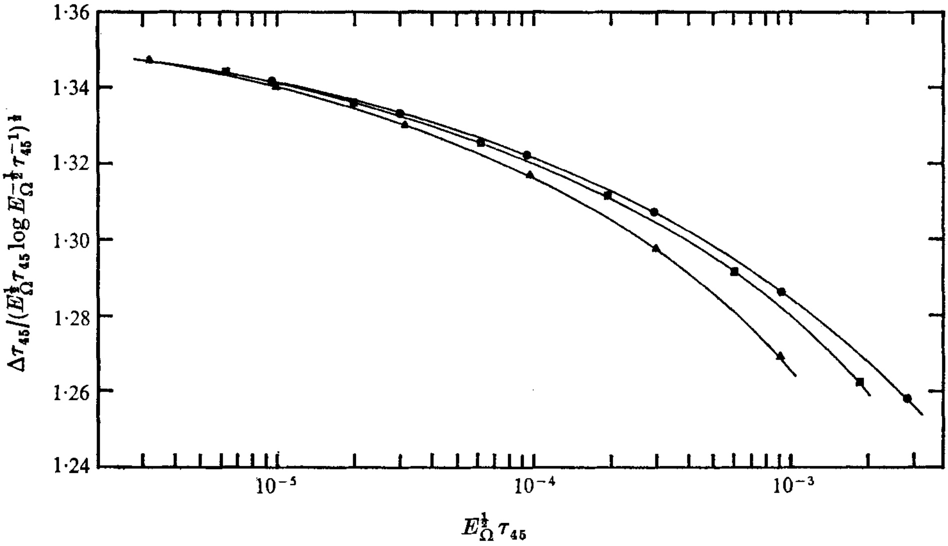

FIGURE 10. Numerical solutions for $\Delta\tau_{45}$. ▲, $x = 1$; ■, $x = 2$; ● $x = 3$.

Using the preceding results, Greenspan calculated the time it takes for a particle to turn 45° from the initial angle $\frac{1}{2}\pi$. The result shows that the visible front travels faster than the theoretical front (located at $x = \tau$) by a time

$$\Delta\tau_{45} = x-\tau_{45} = O([E_\Omega^{\frac{1}{2}}\tau_{45}\log E_\Omega^{-\frac{1}{2}}\tau_{45}^{-1}]^{\frac{1}{2}}). \qquad (A\,4)$$

In order to test this prediction and determine the proportionality factor, the author performed some numerical integrations of (A 3) for the shear distribution obtained by differentiation of (A 2). Solutions were obtained at the three spatial positions $x = 1$, 2 and 3 for values of E_Ω ranging from 10^{-6} to 10^{-11}. The results, plotted with an expanded vertical scale in figure 10, do confirm the predicted time shift given by (A 4); moreover, the curves clearly demonstrate the independence of x for sufficiently small values of $E_\Omega^{\frac{1}{2}}\tau_{45}$. In the limit $E_\Omega^{\frac{1}{2}}\tau_{45}\rightarrow 0$, an asymptotic constant of proportionality of about 1·36 is anticipated.

Although these one-dimensional calculations do not directly apply to the present experiment, one would hope an order-of-magnitude comparison could be made. Taking $E_\Omega = 10^{-8}$ and $x = 1$ as representative values for the almost-impulsive spin-up measurements in figure 2(c), we use (A 2) to evaluate v and $dv/d\bar{t}$ at τ_{45} when the particles begin to rotate. The results are $v = 0{\cdot}00010$ and $dv/d\bar{t} = (dv/d\tau)\,(d\tau/d\bar{t}) = (0{\cdot}022)\,(0{\cdot}052) = 0{\cdot}0011$. These estimates provide some justification for assuming that both the velocity and its time derivative are vanishingly small when the aluminium flakes first sense the approaching wave front.

REFERENCES

BRAYTON, D. B. 1969 A simple laser, Doppler shift, velocimeter with self-aligning optics. *AEDC-TR*-70-45.

CALDWELL, D. R. & VAN ATTA, C. W. 1970 Characteristics of Ekman boundary layer instabilities. *J. Fluid Mech.* **44**, 79–95.

CERASOLI, C. P. 1975 Free shear layer instability due to probes in rotating source–sink flow. *J. Fluid Mech.* **72**, 559–586.

FALLER, A. J. 1963 An experimental study of the instability of the laminar Ekman boundary layer. *J. Fluid Mech.* **15**, 560–576.

FALLER, A. J. & KAYLOR, R. E. 1965 Investigations of stability and transition in rotating boundary layers. *Dynamics of Fluids and Plasmas* (ed. S. I. Paid), pp. 309–329. Academic.

FALLER, A. J. & KAYLOR, R. E. 1966 A numerical study of the instability of the laminar Ekman boundary layer. *J. Atmos. Sci.* **23**, 466–480.

GOLDSMITH, J. L. & MASON, S. G. 1962 Particle motions in sheared suspensions. XIII. The spin and rotation of disks. *J. Fluid Mech.* **12**, 88–96.

GOLLER, H. & RANOV, T. 1968 Unsteady rotating flow in a cylinder with a free surface. *Trans. A.S.M.E., J. Basic Engng*, **90**, 445–454.

GÖRTLER, H. 1940 Über eine dreidimensionale Instabilität laminarer Grenzschichten an konkaven Wänden. *Nachr. Ges. Wiss.* **2**, 1–26.

GREENSPAN, H. P. & HOWARD, L. N. 1963 On a time dependent motion of a rotating fluid. *J. Fluid Mech.* **17**, 385–404.

GREGORY, N., STUART, J. T. & WALKER, W. S. 1955 On the stability of three-dimensional boundary layers with application to the flow due to a rotating disk. *Phil. Trans.* A **248**, 155–199.

HAMMERLIN, G. 1955 Über das Eigenwertproblem der dreidimensionalen Instabilität Laminarer Grenzschichten an konkaven Wanden. *J. Rat. Mech. Anal.* **4**, 279–321.

INGERSOLL, A. P. & VENEZIAN, G. 1968 Non-linear spin-up of a contained fluid. *Dept. Geolog. Sci., Calif. Inst. Tech., Pasadena, Contribution*, no. 1612.

JEFFERY, G. B. 1922 The motion of ellipsoidal particles immersed in a viscous fluid. *Proc. Roy. Soc.* A **102**, 161–179.

LILLY, D. K. 1966 On the instability of Ekman boundary flow. *J. Atmos. Sci.* **23**, 481–494.

LUDWIEG, H. 1964 Experimentelle Nachprüfung der Stabilitätstheorien für reibungsfreie Stromungen mit schraubenlinienformigen Stromlinien. *Z. Flugwiss.* **12**, 304–309.

MCLEOD, A. R. 1922 The unsteady motion produced in a uniformly rotating cylinder of water by a sudden change in the angular velocity of the boundary. *Phil. Mag.* **44**, 1–14.

MAXWORTHY, T. 1971 A simple observational technique for the investigation of boundary-layer stability and turbulence. *Turbulence Measurements in Liquids* (ed. G. K. Paterson & J. L. Zakin), pp. 32–37. Dept. Chemical Engineering, Univ. Missouri-Rolla.

PEDLOSKY, J. & GREENSPAN, H. P. 1967 A simple laboratory model for the oceanic circulation. *J. Fluid Mech.* **27**, 291–304.

SMITH, A. M. O. 1955 On the growth of Taylor–Görtler vortices along highly concave walls. *Quart. Appl. Math.* **13**, 233–262.

SMITH, N. H. 1947 Exploratory investigations of laminar boundary layer oscillations on a rotating disk. *N.A.C.A. Tech. Note*, no. 1227.

TATRO, P. R. & MOLLO-CHRISTENSEN, E. L. 1967 Experiments on Ekman layer instability. *J. Fluid Mech.* **28**, 531–543.

TILLMANN, W. 1967 Development of turbulence during the build-up of a boundary layer at a concave wall. *Phys. Fluids Suppl.* **10**, S108–111.

VENEZIAN, G. 1970 Non-linear spin-up. *Topics in Ocean Engineering*, **2**, 87–96. Gulf Publishing Co.

WATKINS, W. B. & HUSSEY, R. G. 1976 Spin-up from rest in cylinder. *Phys. Fluids* (in press).

WEDEMEYER, E. H. 1964 The unsteady flow within a spinning cylinder. *J. Fluid Mech.* **20**, 383–399.

WEIDMAN, P. D. 1973 On the spin-up and spin-down of a contained fluid. Ph.D. thesis, Dept. Aerospace Engineering, University of Southern California, Los Angeles.

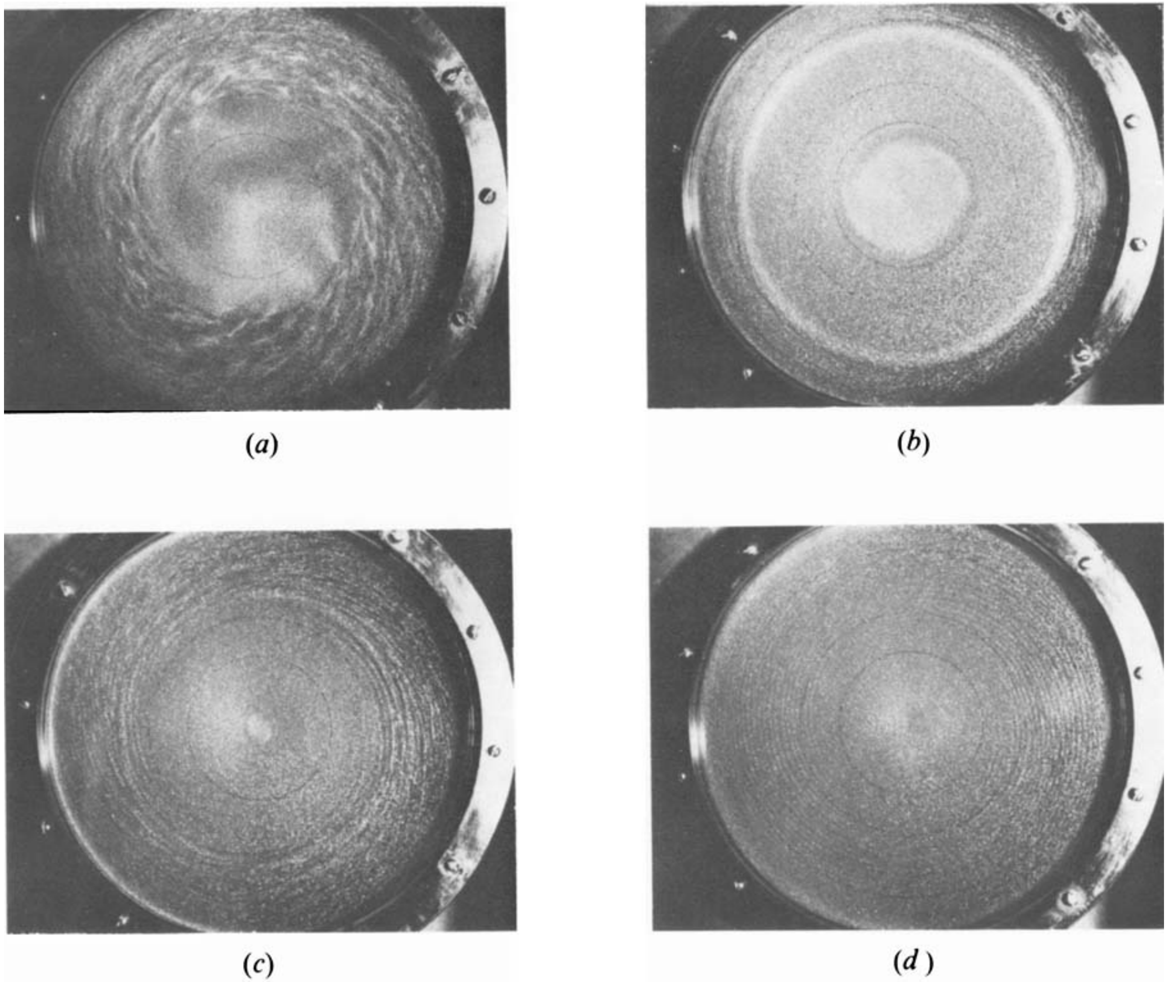

FIGURE 3. Photographs of the flow patterns in the Ekman boundary layer during spin-up from rest at $E_\alpha = 7{\cdot}64 \times 10^{-6}$; cylinder rotation is clockwise. (a) $\bar{t} = 0{\cdot}18$, (b) $\bar{t} = 0{\cdot}43$, (c) $\bar{t} = 0{\cdot}79$, (d) $\bar{t} = 1{\cdot}04$.